



Maximilian Krause · Thomas Böhlke 

Stochastic evaluation of stress and strain distributions in duplex steel

Received: 19 October 2020 / Accepted: 16 February 2021
© The Author(s) 2021

Abstract Austenite–ferrite duplex steels generally consist of two differently textured polycrystalline phases with different glide mechanisms. For estimating the effective mechanical behavior of heterogeneous materials, there exist well established approaches, two of which are the classes of mean-field and full-field methods. In this work, the local fields resulting from these different approaches are compared using analytical calculations and full-field simulations. Duplex steels of various textures measured using X-ray diffraction are considered. Special emphasis is given to the influence of the crystallographic texture on the stress and strain distributions.

Keywords Maximum entropy method · Linear thermoelasticity · Heterogeneous materials · Homogenization · Statistical second moments

1 Introduction

X2CrNiN23-4 is a duplex steel consisting of ferritic and austenitic phases in equal volume fraction. As these phases exhibit a contrast in both elastic and plastic properties, any macroscopic load acts differently on the two phases, increasing the difficulty of simulation. Furthermore, plastic deformations induce residual stresses which are balanced on the macroscopic scale, but may, through their effects on the microstructure, affect the macroscopic behavior.

In order to accurately describe the strain and stress distributions in a heterogeneous material, phase-wise statistics are necessary. Statistical moments of first- and second-order are often considered, as these are particularly accessible using analytical approximations.

In this context, the two main methods are homogenization and localization. Homogenization seeks to find a homogeneous effective material behavior to describe the heterogeneous material at the macroscale, linking macroscopic strains with macroscopic stresses. If the entire microstructure is available, it is possible to numerically solve the boundary condition problem using for example FE [6] or FFT [15] methods. Should it not be feasible to assemble a representative microstructure or perform the associated computations, homogenization can be achieved using analytical methods, which may be exact for particular microstructures [1], but are more often approximations. An overview of these methods is given by [16] or Torquato [22] and the references therein. These methods generally require only the one-point probability function of material properties, along with some microstructural assumptions. To acquire statistical moments from the homogenized problem, a theory of localization is required.

In the present work, various methods of localization are applied to the austenitic-ferritic duplex steel X2CrNiN23-4. Among these are numerical simulations, common analytical approaches and the maximum

M. Krause · T. Böhlke (✉)
Chair for Continuum Mechanics, Institute of Engineering Mechanics, Karlsruhe Institute of Technology (KIT), 76131 Karlsruhe, Germany
E-mail: thomas.boehlke@kit.edu

entropy method due to Kreher and Pompe [10]. By investigating the distributions of stresses and strains for three increasingly complicated models, the viability of the methods can be compared. Furthermore, the approach of modeling each of the polycrystalline duplex steel phases as a homogeneous material used by, e.g., Lani et al. [12] or Hofinger et al. [7] is evaluated.

The manuscript is organized as follows. In Sect. 2, some relevant results of continuum mechanics are recapitulated, including the method of maximal information entropy. In Sect. 3, three different models of duplex steel increasing in complexity are considered using the methods available. In Sect. 4, the results are summarized.

Notation A symbolic tensor notation is preferred throughout the text. Scalars are denoted by light-face type characters, e.g., a, b, α, β, W . First-order tensors are denoted by bold-face type lower case Latin characters, e.g., \mathbf{x}, \mathbf{y} . Second-order tensors are denoted by bold upper case Latin characters and Greek characters, e.g., $\mathbf{A}, \boldsymbol{\sigma}, \boldsymbol{\varepsilon}$. Fourth-order tensors are denoted by blackboard bold upper case Latin characters, e.g., \mathbb{C}, \mathbb{S} . The scalar product between first-, second-, and fourth-order tensors is denoted as $\mathbf{a} \cdot \mathbf{b}$, $\mathbf{A} \cdot \mathbf{B}$, and $\mathbb{A} \cdot \mathbb{B}$, respectively. The tensor product is denoted by \otimes . The Rayleigh product is denoted by $\mathbf{Q} \star \mathbb{A}$; it denotes a rotation of the tensor \mathbb{A} , if \mathbf{Q} is a proper orthogonal tensor ($\mathbf{Q} \in Orth^+$). The components of any tensor with respect to its orthonormal basis are denoted by a_i, A_{ij}, C_{ijkl} , respectively, for first-, second- and fourth-order tensors with the corresponding bases $\{\mathbf{e}_i\}$, $\{\mathbf{e}_i \otimes \mathbf{e}_j\}$ and $\{\mathbf{e}_i \otimes \mathbf{e}_j \otimes \mathbf{e}_k \otimes \mathbf{e}_l\}$. Einstein's summation convention is applied wherever this index notation is used. The identity on symmetric second-order tensors is denoted by \mathbb{I}^S and has the components $I_{ijkl}^S = (\delta_{ik}\delta_{jl} + \delta_{il}\delta_{jk})/2$. It can be decomposed into the projectors $\mathbb{P}_1 = \mathbf{1} \otimes \mathbf{1}/3$ and $\mathbb{P}_2 = \mathbb{I}^S - \mathbb{P}_1$. A stiffness tensor \mathbb{C} is a positive definite fourth-order tensor with minor and major symmetries, i.e., $C_{ijkl} = C_{jikl} = C_{klij}$. The linear map of a second-order tensor over a fourth-order tensor is denoted by $\mathbb{C}[\boldsymbol{\varepsilon}]$. A bilinear form $\boldsymbol{\varepsilon} \cdot \mathbb{C}[\boldsymbol{\varepsilon}]$ is computed as $\varepsilon_{ij}C_{ijkl}\varepsilon_{kl}$. The inverse of a fourth-order tensor with respect to \mathbb{I}^S is denoted by \mathbb{C}^{-1} . The expectation value of a quantity ψ is denoted as $\langle \psi \rangle$. Effective quantities are denoted by a bar, e.g., $\bar{\psi}$.

2 Theory

2.1 Exact analytical formulas for two-phase composites

The phase-wise mean values of stresses and strains can be calculated exactly for affine linear elastic two-phase composites. In such composites, stress-free strains or eigenstrains $\boldsymbol{\varepsilon}^\theta$ are present, which represent, e.g., thermal or plastic deformations. In the examples considered here, they are caused by prior plastic deformations. Assuming zero stress-free strains yields the local strain field $\boldsymbol{\varepsilon}^I$. By evaluating the equations $\langle \boldsymbol{\varepsilon} \rangle = \bar{\boldsymbol{\varepsilon}}$ and $\langle \mathbb{C}[\boldsymbol{\varepsilon}] \rangle = \mathbb{C}[\bar{\boldsymbol{\varepsilon}}]$, the phasewise mean of the strain field is obtained:

$$\langle \boldsymbol{\varepsilon}^I \rangle_1 = \frac{1}{c_1} (\mathbb{C}_1 - \mathbb{C}_2)^{-1} (\bar{\mathbb{C}} - \mathbb{C}_2) \bar{\mathbb{C}}^{-1} [\bar{\boldsymbol{\sigma}}], \quad (1)$$

where the other phase may be calculated by swapping the indices 1 and 2. In the case of vanishing effective stress, strain field $\boldsymbol{\varepsilon}^{II}$ results with the phasewise mean:

$$\begin{aligned} \langle \boldsymbol{\varepsilon}^{II} \rangle_1 &= \frac{1}{c_1} (\mathbb{C}_2 - \mathbb{C}_1)^{-1} [\langle \mathbb{C}[\boldsymbol{\varepsilon}^\theta] \rangle - \mathbb{C}_2[\bar{\boldsymbol{\varepsilon}}^\theta]] \\ &= \frac{1}{c_1} (\mathbb{C}_2 - \mathbb{C}_1)^{-1} \mathbb{C}_2[\bar{\boldsymbol{\varepsilon}}^\theta - \langle \boldsymbol{\varepsilon}^\theta \rangle] + \boldsymbol{\varepsilon}_1^\theta. \end{aligned} \quad (2)$$

If both eigenstrains and an effective stress are present, the full strain field is given as a superposition of the two. The splitting of $\boldsymbol{\varepsilon}$ into fields I and II is due to Kreher and Pompe [10] and is described in more detail in that work.

From the strain field, the corresponding stress field can be calculated via Hooke's Law. As the stress fields are generally more indicative of material failure, the examples in this work will depict stress fields.

These theoretical results depend only on the validity of the Hill–Mandel condition. Accordingly, all methods discussed in the following are in agreement with these formulas.

An analytical approach for determining the phase-wise second moments of stress and strain can be traced back to Bobeth and Diener [2]. It has been employed by Ponte Castañeda [17] and Lhellec and Suquet [11] among others. A short derivation shall be given here.

The core of the argument is a variation of the effective strain energy by varying the local stiffness, which causes a variation of the local strain:

$$\delta \bar{w} = \frac{1}{2} \left| \frac{\partial}{\partial \gamma} \langle (\boldsymbol{\varepsilon} + \gamma \delta \boldsymbol{\varepsilon}) \cdot (\mathbb{C} + \gamma \delta \mathbb{C}) [\boldsymbol{\varepsilon} + \gamma \delta \boldsymbol{\varepsilon}] \rangle \right|_{\gamma=0}. \quad (3)$$

When any single phase (denominated here as 1) is varied, it follows that:

$$\begin{aligned} 2\delta \bar{w} &= \frac{\partial}{\partial \gamma} \langle (\boldsymbol{\varepsilon} + \gamma \delta \boldsymbol{\varepsilon}) \cdot \mathbb{C} [\boldsymbol{\varepsilon} + \gamma \delta \boldsymbol{\varepsilon}] \rangle \Big|_{\gamma=0} \\ &+ c_1 \frac{\partial}{\partial \gamma} \langle (\boldsymbol{\varepsilon} + \gamma \delta \boldsymbol{\varepsilon}) \cdot (\gamma \delta \mathbb{C}_1) [\boldsymbol{\varepsilon} + \gamma \delta \boldsymbol{\varepsilon}] \rangle \Big|_{\gamma=0}. \end{aligned} \quad (4)$$

Both terms may be rearranged as follows, where \mathbb{E} stands for either fourth-order tensor:

$$\begin{aligned} &\frac{\partial}{\partial \gamma} \langle (\boldsymbol{\varepsilon} + \gamma \delta \boldsymbol{\varepsilon}) \cdot \mathbb{E} [\boldsymbol{\varepsilon} + \gamma \delta \boldsymbol{\varepsilon}] \rangle \Big|_{\gamma=0} \\ &= \frac{\partial}{\partial \gamma} \langle \boldsymbol{\varepsilon} \cdot \mathbb{E} [\boldsymbol{\varepsilon}] \rangle \Big|_{\gamma=0} \quad (\text{I}) \\ &+ \frac{\partial}{\partial \gamma} \langle 2\gamma \delta \boldsymbol{\varepsilon} \cdot \mathbb{E} [\boldsymbol{\varepsilon}] \rangle \Big|_{\gamma=0} \quad (\text{II}) \\ &+ \frac{\partial}{\partial \gamma} \langle \gamma^2 \delta \boldsymbol{\varepsilon} \cdot \mathbb{E} [\delta \boldsymbol{\varepsilon}] \rangle \Big|_{\gamma=0}. \quad (\text{III}) \end{aligned} \quad (5)$$

Term (I) disappears for $\mathbb{E} = \mathbb{C}$. Term (III) disappears after the derivation as $\gamma = 0$. Term (II) is subject to the Hill condition:

$$\langle \delta \boldsymbol{\varepsilon} \cdot \mathbb{E} [\delta \boldsymbol{\varepsilon}] \rangle = \langle \delta \boldsymbol{\varepsilon} \rangle \cdot \langle \mathbb{E} [\delta \boldsymbol{\varepsilon}] \rangle \quad (6)$$

As a variation of the local stiffness does not vary the effective strain, $\langle \delta \boldsymbol{\varepsilon} \rangle = \mathbf{0}$, and term (II) vanishes. From the laws of variational calculus, it follows that:

$$\frac{2}{c_1} \frac{\partial \bar{w}}{\partial \mathbb{C}_1} \cdot \delta \mathbb{C}_1 = \langle \boldsymbol{\varepsilon} \otimes \boldsymbol{\varepsilon} \rangle_1 \cdot \delta \mathbb{C}_1 \quad \forall \delta \mathbb{C}_1. \quad (7)$$

It should be noted that the derivation on the left-hand side must be understood as a derivation over the full (anisotropic) space of major, left and right symmetric fourth-order tensors, regardless of the symmetries of \mathbb{C}_1 . The method is only constrained by the homogenization method employed to calculate \bar{w} , which may be an analytical approximation that does not support materials with arbitrarily anisotropic phases. In that case, only specific isotropic projections of the second moment may be calculated. Such a special case appears, e.g., in Castañeda and Suquet [3]:

$$\mathbb{P}_1 \cdot \langle \boldsymbol{\varepsilon} \otimes \boldsymbol{\varepsilon} \rangle_1 = \frac{2}{3c_1} \frac{\partial \bar{w}}{\partial K_1}, \quad (8)$$

$$\mathbb{P}_2 \cdot \langle \boldsymbol{\varepsilon} \otimes \boldsymbol{\varepsilon} \rangle_1 = \frac{1}{c_1} \frac{\partial \bar{w}}{\partial G_1}. \quad (9)$$

It should be noted that even in statistically isotropic composites with isotropic phases, if the effective strain is not also isotropic, there is no indication why the second moment should be isotropic in general. Hence, such a model approach generally represents a simplification in modeling.

By using the relation between the effective energy and the effective strain and stiffness, Eq. 7 may also take the form:

$$\langle \boldsymbol{\varepsilon} \otimes \boldsymbol{\varepsilon} \rangle_1 = \frac{1}{c_1} \frac{\partial \bar{C}}{\partial \mathbb{C}_1} [\bar{\boldsymbol{\varepsilon}} \otimes \bar{\boldsymbol{\varepsilon}}], \quad (10)$$

where the brackets denote the application of an eighth-order tensor to a fourth-order tensor.

Box 1 MEM solution for linear elastic materials with discrete phases

$$\begin{aligned}
p_1(\mathbb{C}, \boldsymbol{\varepsilon}) &= \sum_{\alpha=1}^n c_{\alpha} \frac{\exp(-\frac{1}{2}(\boldsymbol{\varepsilon} - \boldsymbol{\gamma}_{\alpha}) \cdot \mathbb{K}_{\alpha}^{-1}[\boldsymbol{\varepsilon} - \boldsymbol{\gamma}_{\alpha}])}{\sqrt{(2\pi)^6 \det(\mathbb{K}_{\alpha})}} \\
\mathbb{K}_{\alpha} &= \frac{\mathbb{C}_{\alpha}^{-1}}{6} (\bar{\boldsymbol{\varepsilon}} \cdot (\mathbb{C}_{+} - \bar{\mathbb{C}})(\mathbb{C}_{+} - \mathbb{C}_{-})^{-1}(\bar{\mathbb{C}} - \mathbb{C}_{-})[\bar{\boldsymbol{\varepsilon}}]) \\
\boldsymbol{\gamma}_{\alpha} &= \mathbb{C}_{\alpha}^{-1} \mathbb{C}_{-} (\mathbb{C}_{+} - \mathbb{C}_{-})^{-1} (\mathbb{C}_{+} - \bar{\mathbb{C}})[\bar{\boldsymbol{\varepsilon}}] \\
&\quad + (\mathbb{C}_{+} - \mathbb{C}_{-})^{-1} (\bar{\mathbb{C}} - \mathbb{C}_{-})[\bar{\boldsymbol{\varepsilon}}]
\end{aligned}$$

2.2 Maximum-entropy method

The maximum-entropy method (MEM) pioneered by Kreher and Pompe [10] provides an approximation of the first- and second-order statistical moments of stresses and strains in a multi-phase material, given an effective load, the effective behavior, the phase volume fractions and the behavior of the phases.

The joint probability distribution $p(\boldsymbol{\varepsilon}^{\text{I}}, \boldsymbol{\varepsilon}^{\text{II}}, \mathbb{C}, \boldsymbol{\varepsilon}^{\theta})$ of phase strains $\boldsymbol{\varepsilon}^{\text{I}}$ and $\boldsymbol{\varepsilon}^{\text{II}}$ as well the material properties \mathbb{C} and $\boldsymbol{\varepsilon}^{\theta}$ is the unknown to be solved for. For brevity, the variables will be grouped as a vector \boldsymbol{x} . Even though some macroscopic statistical values such as means or variances are known, there are an infinite number of possible p . According to Jaynes [8], the information entropy or information content of a probability distribution can be calculated as follows:

$$S = - \int p(\boldsymbol{x}) \ln(p(\boldsymbol{x})) d\boldsymbol{x}. \quad (11)$$

The principle of maximal information entropy distinguishes those p which contain a maximum of information. A maximum of random information corresponds to a minimum of determined information. Any such determined information could be formulated as further assumptions about the probability distribution. Therefore, the state of maximal information entropy corresponds to a state of minimal unfounded assumptions. The approach may be formally stated as:

$$\max_p S \quad \text{subject to} \quad F_{\beta}(p) = 0, \quad (12)$$

where F_{β} are functionals representing constraints any p must satisfy.

A solution of maximal entropy is generally an approximation. It does not correspond to the real solution because only the volume fractions and the effective behavior were considered. For example, when considering polycrystals, grain sizes or shapes are not considered explicitly, though they would have an impact on the local strains.

Instead, the constraints applied to the maximization of the entropy are as follows:

- the given effective stresses and effective strains, yielding two tensor-valued constraints for each of the fields I, II
- the given effective plastic energy density, yielding a scalar constraint
- the phase volume fraction or, more generally, marginalized distribution of material properties, yielding a function-valued constraint
- the Hill–Mandel condition for each combination of the fields I and II, yielding four scalar constraints

The optimization can then be carried out analytically, yielding formulas which may be applied to various material classes. When no stress-free strains are present, field II disappears, simplifying the unwieldy general formulas. A short summary of the derivation for this special case is given in “Appendix A”.

For the purpose of this work, two sets of formulas are particularly relevant. Multi-phase linear elastic materials are detailed in box 1. In box 2, formulas for multi-phase linear-elastic polycrystals in terms of the orientation distribution function (ODF) f are detailed. In these formulas, \mathbb{C}_{+} and \mathbb{C}_{-} denote the Voigt [23] and Reuss [18] bounds, respectively. Readers interested in the corresponding formulas including stress-free strains and a more thorough description of the derivation are referred to Krause and Böhlke [9].

Box 2 MEM solution for linear elastic multi-phase polycrystals

$$p_1 = \sum_{\alpha=1}^N \frac{c_{\alpha} f(\mathbf{Q}_{\alpha}) \exp\left(-\frac{1}{2}(\boldsymbol{\varepsilon} - \boldsymbol{\gamma}_{\alpha}) \cdot \mathbb{K}_{\alpha}^{-1}[\boldsymbol{\varepsilon} - \boldsymbol{\gamma}_{\alpha}]\right)}{\sqrt{(2\pi)^6 \det(\mathbb{K})}}$$

$$\mathbb{K}_{\alpha} = \frac{1}{2} d \mathbf{Q}_{\alpha} \star \mathbb{C}_{\alpha}^{-1}$$

$$\boldsymbol{\gamma}_{\alpha} = \mathbf{Q}_{\alpha} \star \mathbb{C}_{\alpha}^{-1}[\boldsymbol{\mu}_{\varepsilon}] + \boldsymbol{\mu}_{\sigma}$$

$$\boldsymbol{\mu}_{\varepsilon} = \mathbb{C}_{-} (\mathbb{C}_{+} - \mathbb{C}_{-})^{-1} (\mathbb{C}_{+} - \bar{\mathbb{C}})[\bar{\boldsymbol{\varepsilon}}]$$

$$\boldsymbol{\mu}_{\sigma} = (\mathbb{C}_{+} - \mathbb{C}_{-})^{-1} (\bar{\mathbb{C}} - \mathbb{C}_{-})[\bar{\boldsymbol{\varepsilon}}]$$

$$d = \frac{1}{3} \bar{\boldsymbol{\varepsilon}} \cdot (\mathbb{C}_{+} - \bar{\mathbb{C}})(\mathbb{C}_{+} - \mathbb{C}_{-})^{-1} (\bar{\mathbb{C}} - \mathbb{C}_{-})[\bar{\boldsymbol{\varepsilon}}]$$

3 Examples

3.1 General setup

In this section, three states of duplex steel are considered. Fully isotropic duplex steel with uniform ODFs in both phases is contrasted with duplex steel whose texture has been measured using X-ray diffraction as described by Simon et al. [20]. As the most complex model of the material, a composite with both measured texture data and plastic strain distributions obtained from full-field simulations is considered.

The MEM results are compared with reference full-field simulations. Solvers based on the fast Fourier transform (FFT) according to the approach introduced by Moulinec and Suquet [15] were used. The conjugate gradient method proposed by Zeman et al. [26] is chosen as an optimization algorithm. Ringing artifacts, also called Gibbs' oscillations, are minimized by relying upon the staggered grid discretization [19]. All calculations were carried out using the FFTW library for Python 3 the FFTW library [5]. Further details on the FFT-based solver used can be found in Wicht et al. [24], Wicht et al. [25].

The polycrystal microstructures used for the simulations were generated via Laguerre tessellation. Each microstructure was 256 voxels wide and contained 8000 grains. The grains were randomly chosen to be of either of two materials, with a target phase volume fraction of 50% each. Each grain has a distinct orientation generated from the measured ODF data.

The microstructures thus generated do not generally permit multiscale homogenization. The distinction into austenite and ferrite phases is present on the same scale as the distinction into separate grains. As Fig. 1 shows, the ferrite crystals are of the same scale as the austenite inclusions in the real microstructure as well. Scale separation cannot be employed, as it is usually considered applicable if multiple orders of magnitude separate the scale of the microstructure from the homogenized material. Therefore, the applicability of the multiscale homogenization is considered on a case-by-case basis in this paper.

In reality, the duplex steel considered consists of clusters of crystals of either type, which in general form anisotropic shapes, often aligned along symmetry axes of manufacturing processes, such as rolling. An example of this can be seen in Fig. 1. This morphological texture introduced by the manufacturing process is not considered in this paper, as only a small deformation rolling process is simulated. Furthermore, the size, shape and orientation of grains may vary depending on the exact location in the part. In the simulations, statistical homogeneity is assumed, eliminating this dependency.

3.2 Isotropic duplex steel

The influence of the crystallographic texture or distribution of crystal orientations is considered by first assuming a textureless state. As the orientation distribution function is uniform in the textureless state, the resulting microstructure is perfectly statistically isotropic, resulting in the isotropy of the effective material properties. Two different approximations of this structure are proposed: one being a polycrystal structure where single crystals of different phases are randomly interspersed, while the other is the same structure with each randomly oriented crystal replaced with an isotropic approximation of the same phase. The second type of structure is

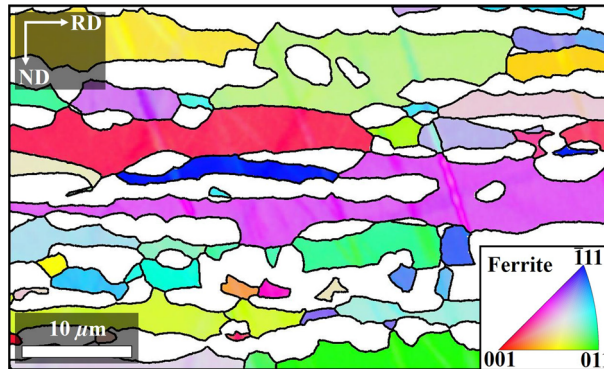


Fig. 1 Duplex microstructure: austenite (white) and ferrite phase (multicoloured) with clearly identifiable rolling direction (RD), as determined by electron backscatter diffraction in [21]

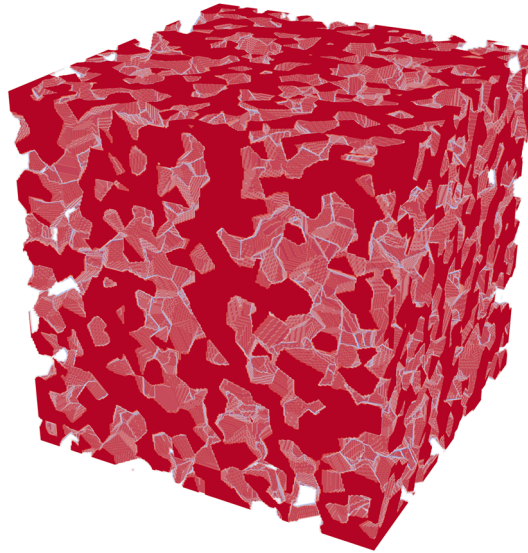


Fig. 2 Model polycrystal microstructure

Table 1 Single crystal material parameters according to Dakhlaoui et al. [4], as well as prehomogenized isotropic parameters, both for Austenite and Ferrite

Parameter	Austenite	Ferrite
C_{1111} in GPa	198	231
C_{1122} in GPa	125	134
C_{1212} in GPa	122	116
\bar{E} in GPa	193	211
$\bar{\nu}$	0.28	0.29

called the prehomogenized structure. A random realization of the phase distribution of these structures can be seen in Fig. 2.

For the cubic single crystal material, parameters based on Dakhlaoui et al. [4] are used, which are shown in Table 1. Furthermore, volume fractions of 50% each are assumed for austenite and ferrite. The geometric mean was shown by Matthies and Humbert [14] to yield plausible effective stiffnesses for polycrystals. The effective values calculated this way are shown in Table 1. These are applied as phase stiffnesses in the prehomogenized structure.

Figure 3 shows the distribution of the stress component in loading direction under a uniaxial effective stress of 100 MPa. The skew of the austenite distribution in particular shows that the MEM, through accumulation of one normal distribution per crystal orientation, can model a non-normal phase stress distribution. A similar

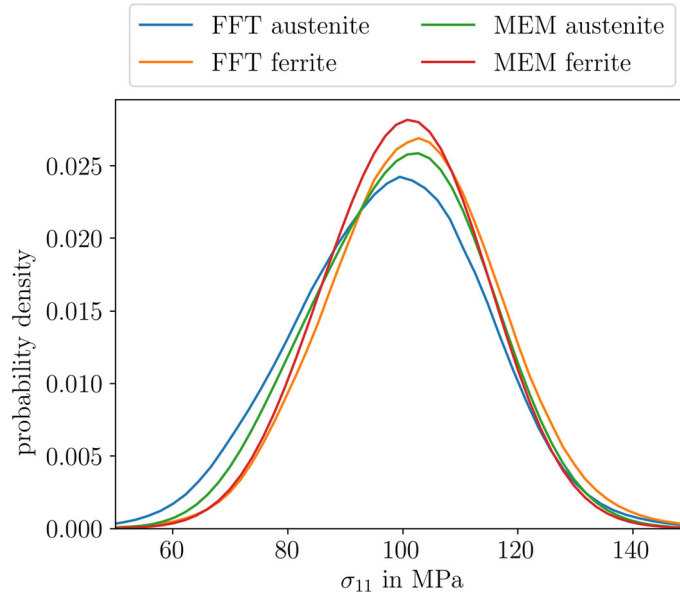


Fig. 3 Distribution of stress in loading direction σ_{11} for polycrystalline duplex steel (macroscopically isotropic)

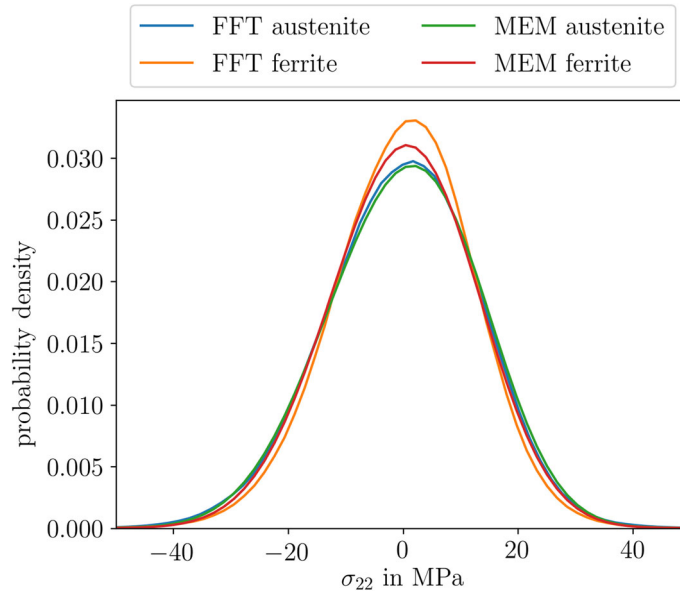


Fig. 4 Distribution of stress orthogonal to loading direction σ_{22} for polycrystalline duplex steel (macroscopically isotropic)

picture presents itself in Fig. 4, which shows the equivalent distribution for a stress component orthogonal to the loading direction.

In Fig. 5, the stress results for the prehomogenized approach with two isotropic phases is shown. In this case, the MEM is constrained to a normal distribution per phase, which does not correspond to the FFT as well as in the full calculation. While the phase mean stresses remain similar, both approaches yield vastly smaller variances compared to the full calculation. This result is confirmed by a numerical evaluation of the analytical second moment as described in Sect. 2.1. In conclusion, the prehomogenization seems unusable for the non-textured model of duplex steel if second moments of stress may impact the result.

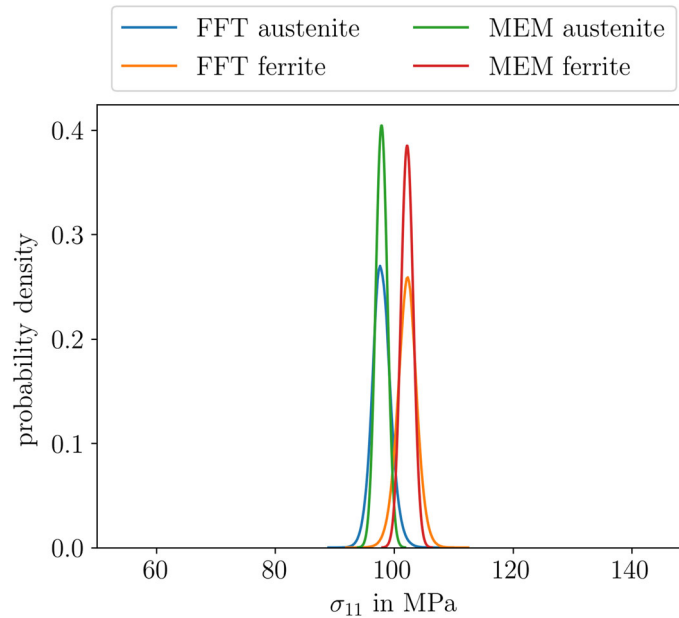


Fig. 5 Distribution of stress in loading direction σ_{11} for prehomogenized duplex steel (isotropic)

3.3 Textured duplex steel

For a more complex model of the duplex steel, texture is considered. Again, there are two approaches: first, the entire polycrystal is considered; then, a prehomogenized version is used as a reduced model. The structures are as described in Sect. 3.2. Texture data measured via X-ray diffraction as described by Simon et al. [20] are used to define the orientations of the single crystals. The single crystal stiffness data are as described in Table 1.

For the prehomogenized stiffness data, a numerical homogenization scheme is used. Both phases are used for single-phase polycrystal calculations of appropriate texture. By applying six orthogonal directions of effective strain and measuring the effective stress, all components of the effective stiffness can be calculated.

The polycrystal stress distribution for an effective stress load of 100 MPa in rolling direction is shown in Fig. 6 for the stress in rolling direction and in Fig. 7 for the stress in the transverse direction. In comparison with the isotropic polycrystal, the elastic contrast between phases is more pronounced, as evident in the mean values of the distributions. While the introduction of texture has caused a slight difference between MEM and FFT results, the MEM can still be considered a good approximation.

In Fig. 8, the distribution of stress in rolling direction for the prehomogenized model can be seen. As in the non-prehomogenized version, MEM and FFT results agree with each other. Additionally, the results are close to the non-prehomogenized version both in phase means and phase variances. Prehomogenization is a valid approach for the textured duplex model, yet not for the textureless version. A possible explanation for this result lies in the effect of phase contrast on strain and stress variances. With increased contrast, the variances rise. Both prehomogenized models cannot capture the contrast between crystals of different orientations. However, while the homogenized textureless model shows only negligible contrast between the phases, the homogenized textured model retains significant contrast as the different textures cause different anisotropic stiffnesses. Therefore, the prehomogenization more closely predicts the variances of the textured model.

3.4 Rolled duplex steel

To more closely simulate an actual sample of duplex steel, texture must be considered in concordance with plastic strains. Data for this model are acquired via a full-field simulation employing crystal plasticity with a Chaboche potential (cf. chapter 6 of Lemaitre and Chaboche [13]) and a linear-exponential hardening law. The models are fit to the results of Simon et al. [21]. Again, the texture data of Simon et al. [20] is used.

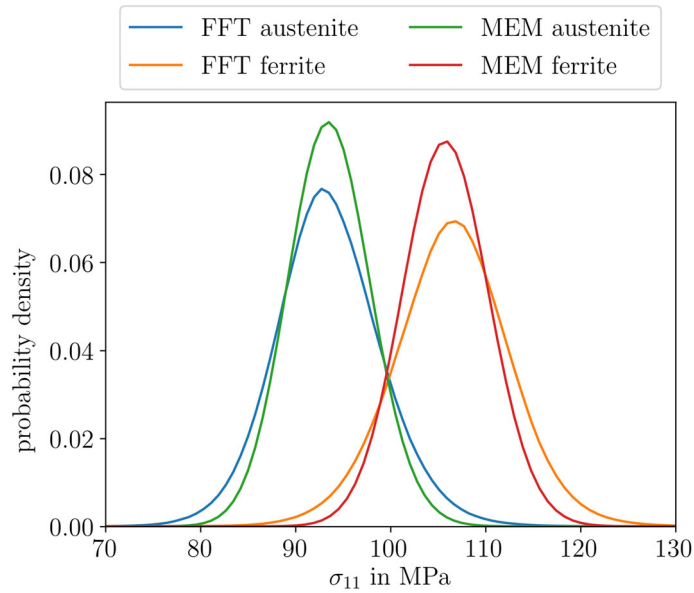


Fig. 6 Distribution of stress in loading direction σ_{11} for polycrystalline duplex steel (textured)

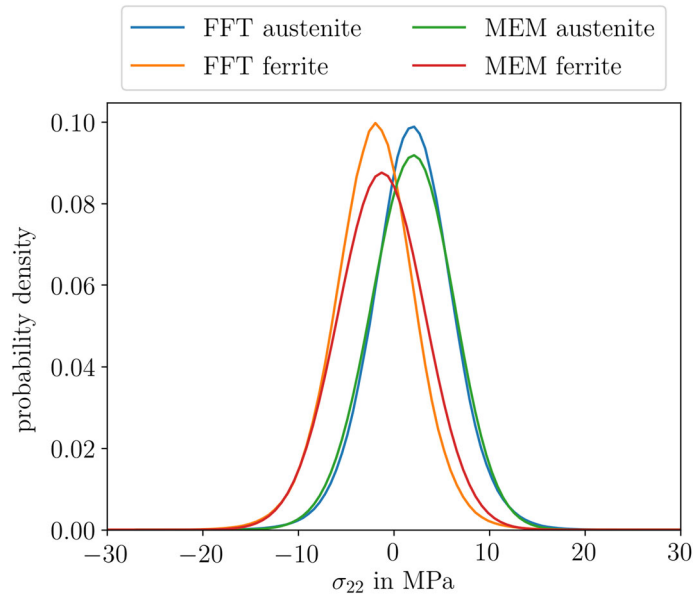


Fig. 7 Distribution of stress orthogonal to loading direction σ_{22} for polycrystalline duplex steel (textured)

A compressive strain of 3% is applied in the direction normal to the rolling, while the other directions are stress-free. This loading is then removed.

The MEM approximation is tailored to fit the unloaded state as closely as possible. The effective stiffness, the effective strain and the effective inelastic energy are taken from the numerical simulation. Using the plastic strains from the simulation, each voxel is modeled as a phase in the MEM.

The results are shown in Fig. 9 for the stress in normal direction and in Fig. 10 for the stress in the transverse direction. These statistics describe the full stress field caused by the plastic strains of an approximated rolling process after the loading is removed, which is equivalent to the eigenstresses of first, second and third kind. The MEM solution is similar to the full-field simulation, particular orthogonal to the loading direction. In loading direction, the stress distribution in the austenite phase deviates markedly from a normal distribution, which may be connected to the deviation between the MEM and the full-field reference solution.

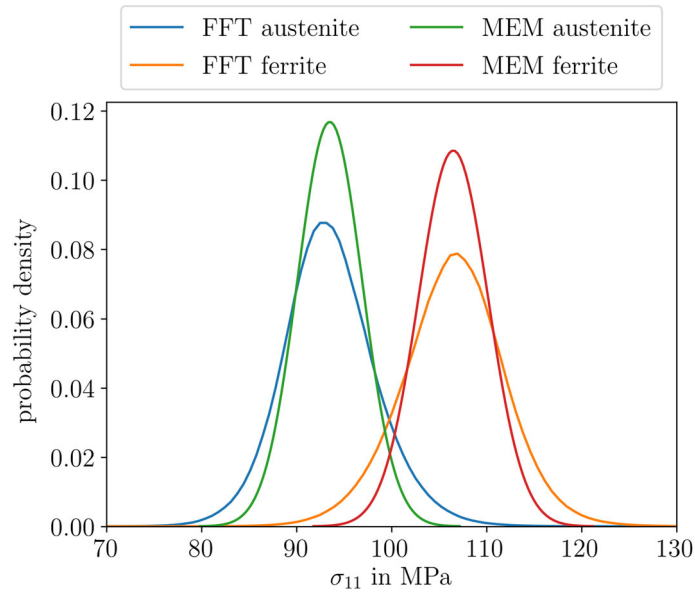


Fig. 8 Distribution of stress in loading direction σ_{11} for prehomogenized duplex steel (textured)

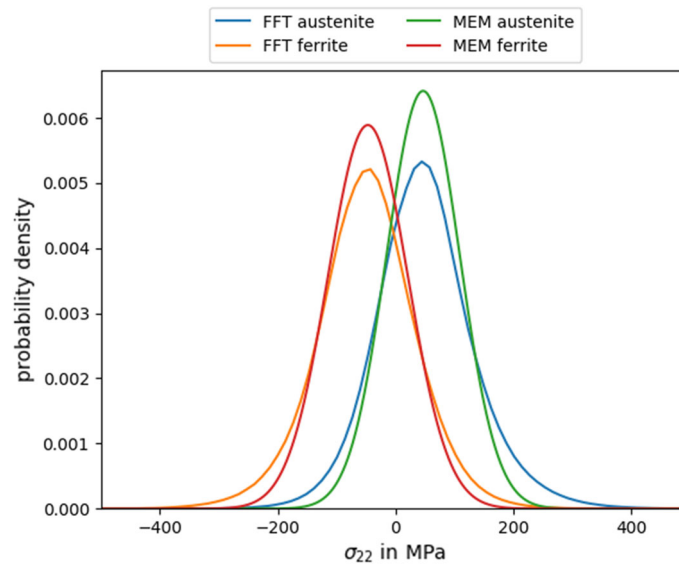


Fig. 9 Distribution of stress orthogonal to loading direction σ_{22} for polycrystalline duplex steel (rolled)

In conclusion, given the eigenstrains, the effective stiffness, the effective inelastic strain and the effective inelastic energy, the MEM yields an approximation of the eigenstresses of first, second and third kind which is not as close as in the purely elastic case. Differences between the methods are due to the fact that the full-field solution is not necessarily the solution of maximal entropy, meaning that further assumptions such as the grain size are missing from the maximum entropy approach.

Considering the limitations of measurement methods such as XRD, a simplified model in which the plastic strains are prehomogenized over each grain is considered. As the stiffness in each grain is homogeneous, the bounds on the effective plastic strain coincide, such that the plastic strain in each grain is replaced by the mean of the plastic strain calculated in the full-field simulation. The effective values of the non-prehomogenized full-field solution are used, leading to MEM results which significantly deviate from the non-prehomogenized full-field simulation in the phase means, as can be seen in Figs. 11 and 12. Models which assume constant eigenstrains in the grains, including the models used in the post-processing of experimental data, may therefore diverge strongly from the true results.

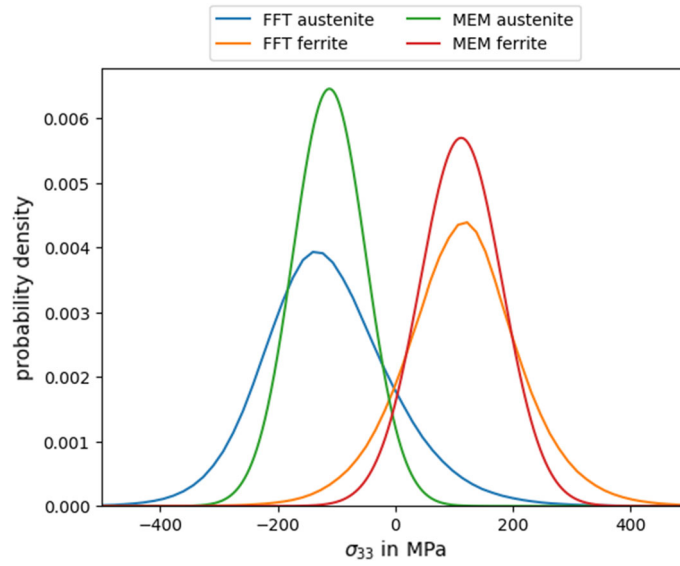


Fig. 10 Distribution of stress in loading direction σ_{33} for polycrystalline duplex steel (rolled)

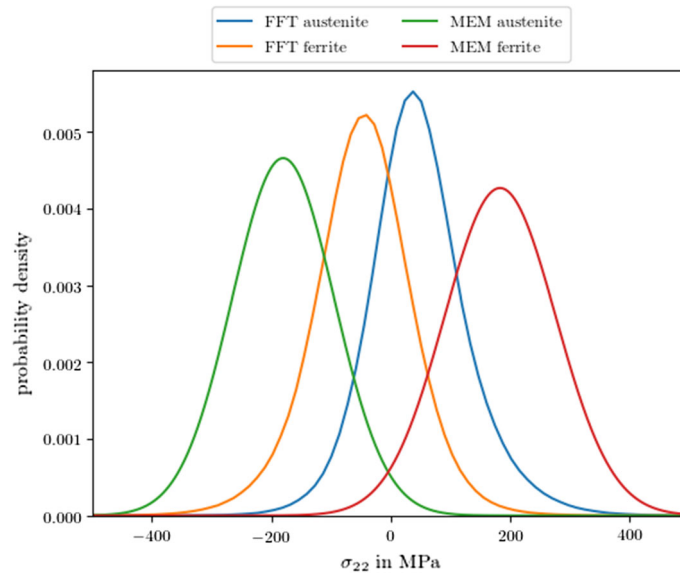


Fig. 11 Distribution of stress orthogonal to loading direction σ_{22} for polycrystalline duplex steel (rolled), prehomogenized in each grain

Attempting to prehomogenize the two phases and their plastic eigenstrains to one phase each distorts the results sufficiently that both full-field simulation and MEM agree on resulting stresses on the order of 1 MPa, less than a hundredth of the non-homogenized values.

4 Conclusions

In the present work, numerical full-field simulations and the maximum entropy approximation were used to estimate statistics of local stress and strain fields in duplex steels. By comparing increasingly detailed models, it was shown that:

- texture has a noticeable effect on the stress statistics of duplex steel, in this particular case increasing the stress contrast in phase means while decreasing the variances;

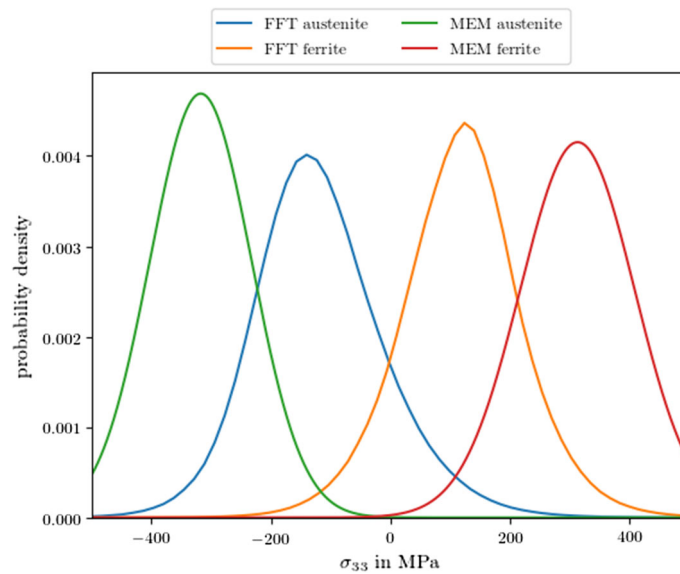


Fig. 12 Distribution of stress in loading direction σ_{33} for polycrystalline duplex steel (rolled), prehomogenized in each grain

- plastic strains resulting from a 3% deformation similar to a rolling process induce eigenstresses on the order of 100 MPa.

In each case, the maximum entropy approximation produced results close to the full-field simulation if input parameters derived from the full-field simulation were used. This includes the estimation of eigenstresses of first, second and third kind from known inelastic strains. Given an appropriately chosen homogenization method, the maximum entropy method could fulfill this task without input from a full-field simulation.

Additionally, the concept of prehomogenization or multiscale homogenization was evaluated, concluding that without scale separation, the method happens to yield plausible results for duplex steels with the particular crystallographic texture considered, but is inaccurate for textureless steels and steels with eigenstrains, underestimating the eigenstresses by orders of magnitude. In the case of textured steels with eigenstrains, even a prehomogenization on the grain level strongly affects the results.

Acknowledgements This research was funded by the German Research Foundation (DFG) within the Priority Programme SPP2013 'Targeted Use of Forming Induced Residual Stresses in Metal Components' (Bo 1466/14-2). The support by the German Research Foundation (DFG) is gratefully acknowledged.

Funding Open Access funding enabled and organized by Projekt DEAL.

Open Access This article is licensed under a Creative Commons Attribution 4.0 International License, which permits use, sharing, adaptation, distribution and reproduction in any medium or format, as long as you give appropriate credit to the original author(s) and the source, provide a link to the Creative Commons licence, and indicate if changes were made. The images or other third party material in this article are included in the article's Creative Commons licence, unless indicated otherwise in a credit line to the material. If material is not included in the article's Creative Commons licence and your intended use is not permitted by statutory regulation or exceeds the permitted use, you will need to obtain permission directly from the copyright holder. To view a copy of this licence, visit <http://creativecommons.org/licenses/by/4.0/>.

Compliance with ethical standards

Conflict of interest The authors declare that they have no conflict of interest.

Appendix A: Derivation of the linear elastic MEM

The derivation of the analytical solution of maximum entropy shall be summarized for the simple case of linear elasticity without stress-free strains. In that case, $\boldsymbol{\varepsilon}^1 = \boldsymbol{\varepsilon}$ and the probability distribution to be solved for is

$p(\boldsymbol{\varepsilon}, \mathbb{C})$. The entropy functional follows as:

$$S = - \iint p(\boldsymbol{\varepsilon}, \mathbb{C}) \ln(p(\boldsymbol{\varepsilon}, \mathbb{C})) d\boldsymbol{\varepsilon} d\mathbb{C}. \quad (13)$$

The maximization of that functional involves the following constraints:

$$\langle \boldsymbol{\varepsilon} \rangle = \bar{\boldsymbol{\varepsilon}}, \quad \langle \mathbb{C}[\boldsymbol{\varepsilon}] \rangle = \bar{\mathbb{C}}[\bar{\boldsymbol{\varepsilon}}], \quad (14)$$

$$\langle \boldsymbol{\varepsilon} \cdot \mathbb{C}[\boldsymbol{\varepsilon}] \rangle = \bar{\boldsymbol{\varepsilon}} \cdot \bar{\mathbb{C}}[\bar{\boldsymbol{\varepsilon}}], \quad \int p(\boldsymbol{\varepsilon}, \mathbb{C}) d\boldsymbol{\varepsilon} = p_1^{\mathbb{C}}(\mathbb{C}), \quad (15)$$

where $p_1^{\mathbb{C}}$ is the one-point distribution of phase properties, generally described through phase volume fractions or ODFs.

The right-hand sides of the constraints can be neglected in the following, as they do not contribute after differentiation of the functional. After a scalar product with a Lagrange multiplier from the corresponding vector space, the constraints are added to the entropy functional, resulting in the modified entropy functional:

$$S_{\text{mod}} = \iint p(\boldsymbol{\varepsilon}, \mathbb{C}) (-\ln(p(\boldsymbol{\varepsilon}, \mathbb{C})) + \lambda_{\varepsilon} \cdot \boldsymbol{\varepsilon} + \lambda_{\sigma} \cdot \boldsymbol{\sigma} + \lambda_w \bar{\boldsymbol{\varepsilon}} \cdot \bar{\mathbb{C}}[\bar{\boldsymbol{\varepsilon}}] + \lambda_{\mathbb{C}}(\mathbb{C})) d\boldsymbol{\varepsilon} d\mathbb{C}. \quad (16)$$

The optimization of the functional can then be rephrased as a partial differentiation of the integrand by p , leading to:

$$\ln(p(\boldsymbol{\varepsilon}, \mathbb{C})) = -1 + \lambda_{\varepsilon} \cdot \boldsymbol{\varepsilon} + \lambda_{\sigma} \cdot \boldsymbol{\sigma} + \lambda_w \boldsymbol{\varepsilon} \cdot \mathbb{C}[\boldsymbol{\varepsilon}] + \lambda_{\mathbb{C}}(\mathbb{C}). \quad (17)$$

An exponential form follows:

$$p(\boldsymbol{\varepsilon}, \mathbb{C}) = \exp(-1 + \lambda_{\varepsilon} \cdot \boldsymbol{\varepsilon} + \lambda_{\sigma} \cdot \boldsymbol{\sigma} + \lambda_w \boldsymbol{\varepsilon} \cdot \mathbb{C}[\boldsymbol{\varepsilon}] + \lambda_{\mathbb{C}}(\mathbb{C})). \quad (18)$$

Substitution of the Lagrange multipliers with $\boldsymbol{\gamma} = \mathbb{C}[\boldsymbol{\mu}_{\varepsilon}] + \boldsymbol{\mu}_{\sigma}$ and d leads to a more recognizable normal distribution:

$$p(\boldsymbol{\varepsilon}, \mathbb{C}) = m(\mathbb{C}) \exp\left(\frac{1}{2} d(\boldsymbol{\varepsilon} - \boldsymbol{\gamma}) \mathbb{C}^{-1}[\boldsymbol{\varepsilon} - \boldsymbol{\gamma}]\right), \quad (19)$$

where $m(\mathbb{C})$ contains all parts of the exponential form which do not depend on $\boldsymbol{\varepsilon}$.

The function $m(\mathbb{C})$ and the variables $\boldsymbol{\mu}_{\sigma}$, $\boldsymbol{\mu}_{\varepsilon}$ and d are then determined by evaluating the constraints for this probability distribution, leading to Table 1 when assuming discrete phases and Table 2 for polycrystals.

References

1. Bensoussan, A., Lions, J.L., Papanicolaou, G.: Asymptotic Analysis for Periodic Structures. Vol. 5 of Studies in Mathematics and Its Applications. North-Holland Publishing Company, Amsterdam (1978)
2. Bobeth, M., Diener, G.: Static elastic and thermoelastic field fluctuations in multiphase composites. *J. Mech. Phys. Solids* **35**(2), 137–149 (1987)
3. Castañeda, P.P., Suquet, P.: Nonlinear composites. In: *Advances in Applied Mechanics*, pp. 171–302. Elsevier (1997)
4. Dakhlaoui, R., Baczmański, A., Braham, C., Wroński, S., Wierzbowski, K., Oliver, E.: Effect of residual stresses on individual phase mechanical properties of austeno-ferritic duplex stainless steel. *Acta Mater.* **54**(19), 5027–5039 (2006)
5. Frigo, M., Johnson, S.G.: The design and implementation of FFTW3. In: *Proceedings of the IEEE 93* (2), 216–231, special issue on “Program Generation, Optimization, and Platform Adaptation” (2005)
6. Guedes, J.-M., Kikuchi, N.: Preprocessing and postprocessing for materials based on the homogenization method with adaptive finite element methods. *Comput. Methods Appl. Mech. Eng.* **83**(2), 143–198 (1990)
7. Hofinger, J., Erdle, H., Böhlke, T.: Prediction of residual stresses of second kind in deep drawing using an incremental two-scale material model. *Philos. Mag.* **100**(22), 2836–2856 (2020)
8. Jaynes, E.T.: *Statistical Physics*. Vol. 3 of Brandeis Summer Institute Lectures in Theoretical Physics. W.A. Benjamin Inc., New York (1963)
9. Krause, M., Böhlke, T.: Maximum-entropy based estimates of stress and strain in thermoelastic random heterogeneous materials. *J. Elast.* **141**(2), 321–348 (2020)

10. Kreher, W., Pompe, W.: Internal Stresses in Heterogeneous Solids. Vol. 9 of Physical Research. Akademie-Verlag, Berlin (1989)
11. Lahellec, N., Suquet, P.: On the effective behavior of nonlinear inelastic composites: I. Incremental variational principles. *J. Mech. Phys. Solids* **55**(9), 1932–1963 (2007)
12. Lani, F., Furnémont, Q., Rompaey, T.V., Delannay, F., Jacques, P., Pardoën, T.: Multiscale mechanics of TRIP-assisted multiphase steels: II. Micromechanical modelling. *Acta Mater.* **55**(11), 3695–3705 (2007)
13. Lemaitre, J., Chaboche, J.-L.: *Mechanics of Solid Materials*. Cambridge University Press, Cambridge (1990)
14. Matthies, S., Humbert, M.: On the principle of a geometric mean of even-rank symmetric tensors for textured polycrystals. *J. Appl. Crystallogr.* **28**(3), 254–266 (1995)
15. Moulinec, H., Suquet, P.: A numerical method for computing the overall response of nonlinear composites with complex microstructure. *Comput. Methods Appl. Mech. Eng.* **157**(1), 69–94 (1998)
16. Nemat-Nasser, S., Hori, M.: *Micromechanics: Overall Properties of Heterogeneous Materials*. North-Holland, Amsterdam (1993)
17. Ponte Castañeda, P.: Second-order homogenization estimates for nonlinear composites incorporating field fluctuations: I-theory. *J. Mech. Phys. Solids* **50**(4), 737–757 (2002)
18. Reuss, A.: Berechnung der Fließgrenze von Mischkristallen auf Grund der Plastizitätsbedingung für Einkristalle. *ZAMM Zeitschrift für Angewandte Mathematik und Mechanik* **9**(1), 49–58 (1929)
19. Schneider, M., Ospald, F., Kabel, M.: Computational homogenization of elasticity on a staggered grid. *Int. J. Numer. Methods Eng.* **109**, 693–720 (2016)
20. Simon, N., Erdle, H., Walzer, S., Gibmeier, J., Böhlke, T., Liewald, M.: Phase-specific residual stresses induced by deep drawing of lean duplex steel: measurement vs. simulation. *Prod. Eng.* **13**(2), 227–237 (2019)
21. Simon, N., Krause, M., Heinemann, P., Erdle, H., Böhlke, T., Gibmeier, J.: Phase-specific strain hardening and load partitioning of cold rolled duplex stainless steel x2crni23-4. *Crystals* **10**(11), 976 (2020)
22. Torquato, S.: *Random Heterogeneous Materials*. Springer, New York (2002)
23. Voigt, W.: Ueber die Beziehung zwischen den beiden Elasticitätsconstanten isotroper Körper. *Ann. Phys.* **274**(12), 573–587 (1889)
24. Wicht, D., Schneider, M., Böhlke, T.: An efficient solution scheme for small-strain crystal-elasto-viscoplasticity in a dual framework. *Comput. Methods Appl. Mech. Eng.* **358**, 112611 (2020)
25. Wicht, D., Schneider, M., Böhlke, T.: On quasi-newton methods in fast Fourier transform-based micromechanics. *Int. J. Numer. Methods Eng.* **121**(8), 1665–1694 (2020)
26. Zeman, J., Vondřejc, J., Novák, J., Marek, I.: Accelerating a FFT-based solver for numerical homogenization of periodic media by conjugate gradients. *J. Comput. Phys.* **229**, 8065–8071 (2010)